

---

# Ultra-high energy cosmic rays: from GeV to ZeV

Gustavo Medina Tanco

Instituto de Ciencias Nucleares, UNAM  
& Instituto Astronômico e Geofísico, USP  
gmtanco@gmail.com

## 1 Introduction

Cosmic ray (CR) particles arrive at the top of the Earth's atmosphere at a rate of around  $10^3$  per square meter per second. They are mostly ionized nuclei - about 90% protons, 9% alpha particles traces of heavier nuclei and approximately 1% electrons.

CRs are characterized by their high energies: most cosmic rays are relativistic, having kinetic energies comparable to or somewhat greater than their rest masses. A very few of them have ultra-relativistic energies extending beyond  $10^{20}$  eV (tens of joules).

In this series of lectures, delivered at the 2005 Mexican School of Astrophysics, an overview of the main experimental characteristics of the CR flux and their astrophysical significance is given. Particular emphasis is given to the upper end of the CR energy spectrum.

Unfortunately, due to space limitations, only a fraction of the original content of the lectures is included in the present manuscript. In particular, the production mechanisms are not included and the fundamental topic of anisotropies is only dealt with in a very superficial way.

## 2 Energy spectrum

Thus, the cosmic ray energy spectrum extends, amazingly, for more than eleven orders of magnitude. All along this vast energy span, the spectrum follows a power law of index  $\sim 2.7$ . Therefore, the CR flux decreases approximately 30 orders of magnitude from  $\sim 10^3 \text{ m}^2 \text{ sec}^{-1}$  at few GeV to  $\sim 1 \text{ km}^{-2}$  per century at 100 EeV.

The only spectral features are a slight bending at around few PeV, known as the first knee, another at approximately 0.5 EeV known as the second knee, and a dip extending from roughly the second knee up to beyond 10 EeV,

known as the ankle (see, figure 1). Note that in the right panel the spectrum is multiplied by  $E^3$ , a usual trick to highlight features that otherwise would be almost completely hidden by the rapidly falling flux.

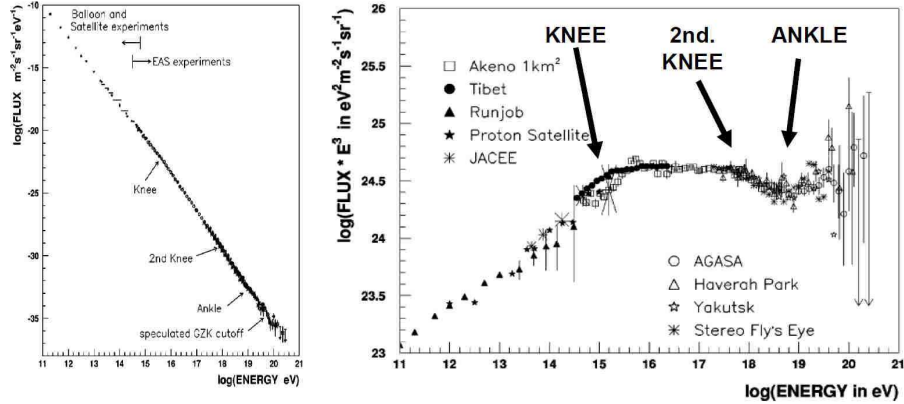


**Fig. 1.** Cosmic ray energy spectrum and its main features: [left] a remarkably uniform power law with [right] few bends knee (few PeV), second knee (0.5 EeV), ankle (EeV to few tens of EeV) and the still poorly known highest energy tail. Adapted from [1]

The second knee has been observed in the vicinity of  $4 \times 10^{17}$  eV by Akeno [2], Fly's Eye stereo [5, 6, 7], Yakutsk [3, 4] and HiRes [10]. The physical interpretation of this spectral feature is uncertain at present. It may be either the end of the Galactic cosmic ray component or the pile-up from pair creation processes due to proton interactions with the cosmic microwave background radiation during propagation in the intergalactic medium.

The ankle, on the other hand, is a broader feature that has been observed by Fly's Eye [5, 6, 7] around  $3 \times 10^{18}$  eV as well as by Haverah Park [8] at approximately the same energy ( $3 \times 10^{18}$  eV). These results have been confirmed by Yakutsk [3, 4] and HiRes [10]. AGASA also observed the ankle, but they locate it at a higher energy, around  $10^{19}$  eV [9]. As with the ankle, more than one physical interpretations are possible, which are intimately related with the nature of the second knee. The ankle may be the transition point between the Galactic and extragalactic components, the result of pair creation by protons in the cosmic microwave background, or the result of diffusive propagation of extragalactic nuclei through cosmic magnetic fields.

## Composition

Certainly, one of the scientifically most relevant pieces of information inside the transition energy interval previously defined, is the precise chemical composition of the primary CR flux as a function of energy.

Several techniques have been used to determine the composition of cosmic rays along the spectrum and, in particular, in the highest energy region [12]: (i) depth of maximum of the longitudinal distribution,  $X_{max}$  [13, 14]; (ii) fluctuations of  $X_{max}$  [15, 16]; (iii) muon density [17, 18]; (iv) steepness of the lateral distribution function [26, 27]; (v) time profile of the signal, in particular rise time of the signal [28]; (vi) curvature radius of the shower front; (vii) multi-parametric analysis, such as principal component analysis and neural networks [29], etc.. Unfortunately, as is frequently the case in physics, whenever several techniques are applied to measure the same physical magnitude, correspondingly, several results are obtained and, not always agreeable among themselves. As will be shown below, this is critical to the understanding of the astrophysics of ultra high energy cosmic rays.

In order to analyze the astrophysical implications of the composition along the second knee/ankle energy region, it is more instructive to start from much lower energies. A significant point is the first knee. Following KASCADE [21], a gradual change in composition is observed through the knee, from a lighter to a heavier composition. The first knee is a broad feature which can be understood as a composition of power law energy spectra with breaks that are in agreement with a rigidity scaling of the knee position.

Therefore, at energies above few times  $10^{16}$  eV, the flux is dominated by iron nuclei. These particles are of Galactic origin and what is being detected is, very likely, the end of the efficiency of supernova remnant shock waves as accelerators as the Larmor radii or characteristic diffusion scale lengths of the nuclei become comparable to the curvature radius of the remnants, breaking down the diffusive approximation. If there are not more powerful accelerators in the Galaxy, the Galactic cosmic ray flux continue dominated exclusively by iron above  $10^{17}$  eV up to the highest energies produced inside the Milky Way. It must be noted that, even if the previous results are quantitatively dependent on the hadronic interaction model used in the data analysis, they are qualitatively solid and there is considerable degree of consensus on the existence of a progressive transition in composition through the knee. At higher energies, the composition has been measured by several experiments in the past, e.g., Haverah Park, Yakutsk, Flys Eye, HiRes-MIA prototype and HiRes in stereo mode (see figure 2).

The  $X_{max}$  data suggest that, above  $10^{16.6}$  eV, the composition changes once more progressively from heavy to light. At the lower limit of this energy interval, the composition is still heavy, i.e., iron dominated, in accordance to Kascade results. Nevertheless, at energies of  $10^{19}$  eV, even if still showing signs of a contamination by heavy elements, it is more consistent with a flux dominated by lighter elements.

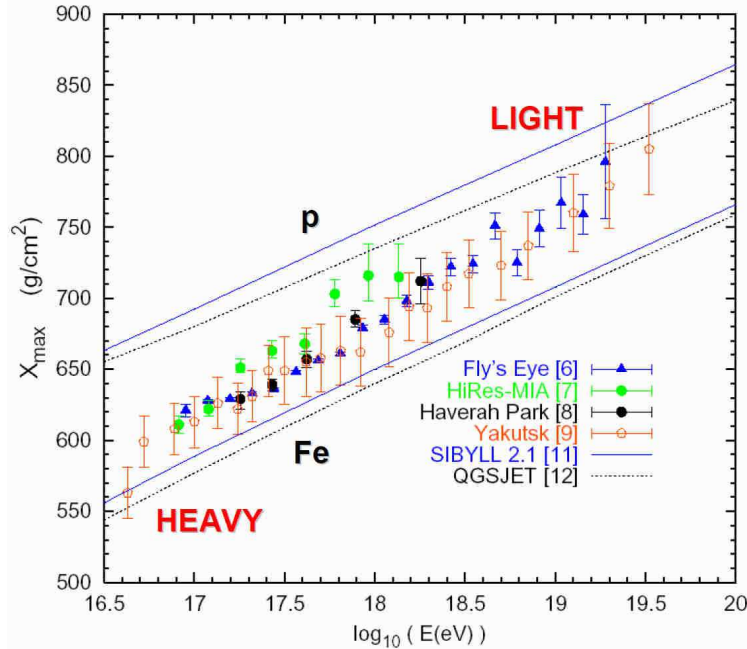


**Fig. 2.** Variation of  $X_{max}$  with energy (elongation rate) showing an apparent change in composition from heavy to light nuclei from  $\sim 30$  PeV to  $\sim 30$  EeV. This variation is at least possibly associated to the transition from Galactic to extragalactic cosmic rays. The lines indicate theoretical expectations corresponding to different hadronic interaction models.

Despite the fact that there is a consensus among most of the experiments about the reality of this smooth transition, there is no consensus about the rate and extent to which the transition occurs. In fact, the combined data from the HiRes-MIA prototype and HiRes in stereo mode, signal to a much more rapid transition from heavy to light composition (see figure 3), starting  $10^{17}$  eV but which would be over by  $10^{18}$  eV [30]. Beyond that point, the composition would remain light and constant.

The later scenario, however, is not supported by the data of other experiments. Haverah Park, for example, shows a predominantly heavy composition up to  $10^{18}$  eV, followed by an abrupt transition to lighter values compatible with HiRes stereo at around  $10^{18}$  eV (see, figure 4.a). Volcano Ranch, even though there is a single experimental point, is compatible with a heavy composition still at  $10^{18}$  eV, somewhat in accordance to Haverah Park data. Akeno (A1), on the other hand, is consistent with a continuation of the gradual transition from the second knee all across the ankle up to at least  $10^{19}$  eV, only reaching there the same light composition that HiRes stereo claims from an order of magnitude below in energy. It must also be noted that above

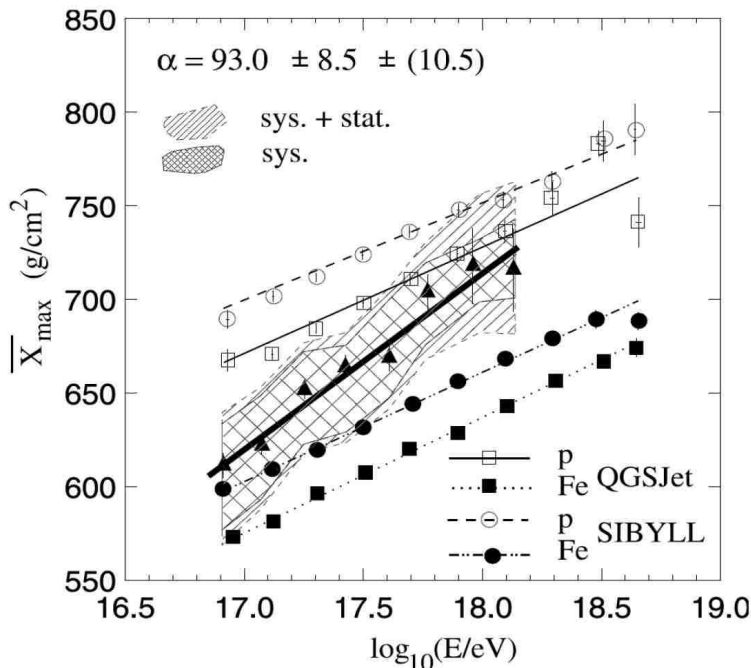
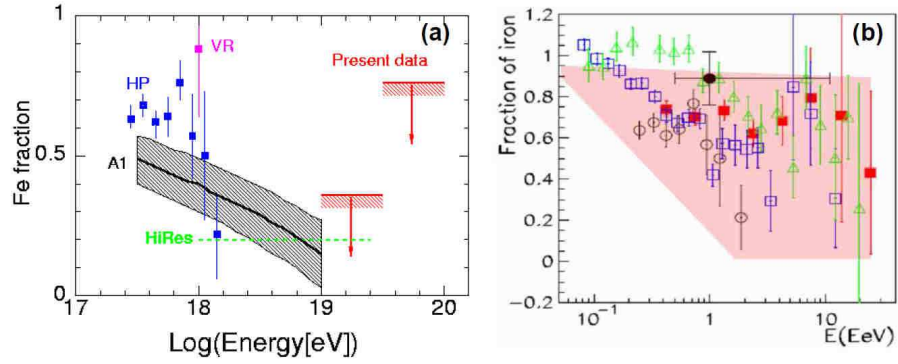


**Fig. 3.** Elongation rate measured by the HiRes-MIA prototype showing a rapid change to a light composition above  $10^{18}$  eV.

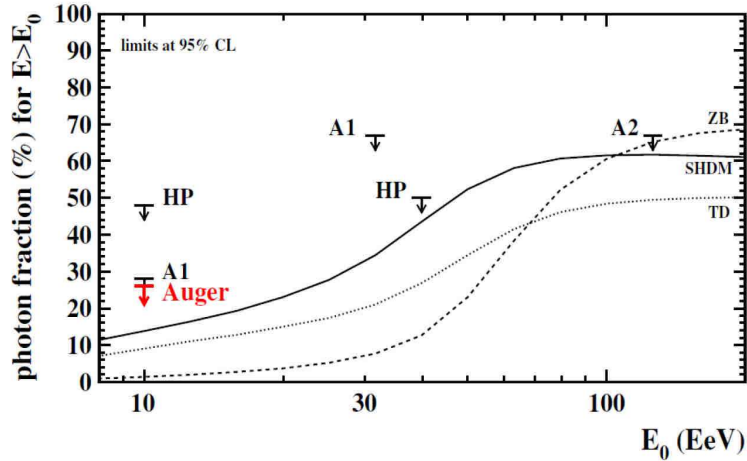
$10^{19}$  eV AGASA is only able to set upper limits for the fraction of iron, but these limits are high enough to leave room for much more complex astrophysical scenarios with a substantial admixture of extragalactic ultra-high energy heavy elements [31].

Figure 4.b shows a compendium of several of the available measurements of composition between  $\sim 10^{17}$  and  $\sim 10^{19}$  eV, with their corresponding error bars, under the simplistic assumption of a binary mixture of protons and iron nuclei. The emerging picture is one complete uncertainty, which has deep practical implications and imposes severe limitations to theoretical efforts.

At energies beyond  $\sim 10$  EeV the composition is essentially unknown. However, it seems compatible with hadrons even if some photon contribution cannot be discarded [32, 33, 34] (see figure 5). Although it is implicitly regarded as purely protonic in many theoretical works, only upper limit exists for the iron fraction (e.g., 4.b) and therefore not much can be said until more accurate measurements are made available by new generation experiments like Auger and TA.



**Fig. 4.** (a) Variation of the iron fraction inside the transition energy interval for various experiments. (b) Idem, highlighting the uncertainties in composition inside the region encompassing the second knee and the ankle: literally almost any abundance of iron is allowed (adapted from [27]).



**Fig. 5.** Upper limits (95% CL) on cosmic-ray photon fraction for Auger [34], AGASA (A1) [32], (A2) [33] and Haverah Park (HP) [35, 36] data compared to some estimates based on TOP-DOWN models [37]. (Reproduced from [34]).

### 3 Galactic propagation

The fundamental question of cosmic ray physics is, "Where do they come from?" and in particular, "How are they accelerated to such high energies?". These are difficult questions not fully answered after almost a century of history of the field.

Some very general hints can be obtained, however, through very simple arguments. The interstellar and intergalactic mediae are magnetized and, being charged, the CR are forced to interact with these fields.

From the point of view of propagation of charged particles, the Galaxy behaves as a magnetized volume, where the field is structured on scales of kpc, with typical intensities of the order of some few micro Gauss.

The Larmor radius of a nucleus of charge  $Ze$  can be conveniently parameterized as:

$$r_{L,kpc} \approx \frac{1}{Z} \times \left( \frac{E_{EeV}}{B_{\mu G}} \right) \quad (1)$$

where  $E_{EeV}$  is the energy of the particle in units of  $10^{18}$  eV and  $r_{L,kpc}$  is expressed in kpc.

Equation (1) clearly shows that, given the typical intensity of the magnetic fields present in the interstellar medium (ISM), nuclei with energies below some few tens of EeV, regardless of their charge, have Larmor radii much smaller than the transversal dimensions of the magnetized Galactic disk. They must, therefore, propagate diffusively inside the ISM. This transforms the Galaxy in an efficient confinement region for charged particles with energies below the second knee. The confinement region is a flattened disk of approximately 20 kpc of radius and thickness of the order of a few hundreds of pc.

Consequently, from the lowest energies and up to the second knee, the Galaxy is undoubtedly the source of the cosmic ray particles and of their kinetic energy. There is not a consensus about the actual source of the particles in itself, but the two main lines of thought propose either nuclei pre-accelerated at the chromospheres of normal F and G type stars or ambient electrically charged nuclei condensed in the dense winds of blue or red giant stars [38, 39]. On the other hand, several acceleration mechanism must be at play but it is widely expected that the dominant one is first order Fermi acceleration at the vicinity of supernova remnant shock waves. Nevertheless, theoretically, the Galactic accelerators should become inefficient between  $\sim 10^{17}$  to  $\sim 10^{18}$  eV. This upper limit could be extended to  $\sim 10^{19}$  eV if additional mechanisms were operating in the Galaxy, e.g., spinning inductors associated with compact objects or cataclysmic events like acceleration of iron nuclei by young strongly magnetized neutron stars through relativistic MHD winds [40].

At energies above the second knee, particles start to be able to travel from the nearest extragalactic sources in less than a Hubble time. Consequently, at some point above  $10^{17.5}$  eV a sizable cosmic ray extragalactic component should be detectable and become dominant above  $10^{19}$  eV. Therefore, it is expected that the cosmic ray flux detected between the second knee and the ankle of the spectrum be a mixture of a Galactic and an extragalactic flux, highlighting the astrophysical richness and complexity of the region.

The type of propagation strongly depends on the charge of the corresponding nucleus.

Protons with energies  $\gtrsim 10^{17}$  eV have gyroradii comparable or larger than the transversal dimensions of the effective confinement region and, therefore, can easily escape from the Galaxy. On the other end of the mass spectrum, just the opposite occurs for iron nuclei that, even at energies of the order of  $10^{19}$  eV, have gyroradii  $< 10^2$  pc and must be effectively confined inside the magnetized interstellar medium.

The previous results are based only on the consideration of the regular component of the Galactic magnetic field. However, there exist a superimposed turbulent component whose intensity is at least comparable to that of the regular field. Its spectrum seems to be of the Kolmogorov type, extending from the smallest scaled probed,  $\sim 10^0$  pc, to  $L_c \sim 100$  pc, the correlation length of the turbulent field.

Wave-particle interactions between cosmic rays and MHD turbulence are resonant for wavelengths of the order of the Larmor radius,  $\lambda \sim r_L$ . This means that, for a nucleus of charge  $Z$ , a critical energy can be defined,

$$r_{L,kpc} \approx \frac{1}{Z} \times \left( \frac{E_{EeV}}{B_{\mu G}} \right) \approx L_c \quad , \quad L_c \approx 10^2 pc \quad \Rightarrow \quad E_{c,EeV} \approx 0.5 \times Z \quad (2)$$

below which modes resonant with the particle gyroradius exist that are able to efficiently scatter the particle in pitch angle. Consequently, at energies below  $E_c$  the diffusion coefficient is small enough for the particles trajectory to be diffusive. At energies above  $E_c$ , on the other hand, the propagation is essentially ballistic.

Due to the interaction with the turbulent magnetic component, protons experience a propagation regime very different than iron nuclei inside the ankle energy region. Protons propagate ballistically in the interstellar medium above  $\sim 3 \times 10^{17}$  eV, while iron nuclei propagate diffusively even at energies  $\gtrsim 10^{19}$  eV.

Therefore, along the energy region extending from the second knee up to almost the end of the ankle, all nuclei from p to Fe, i.e.  $1 < Z < 26$ , experience a transition in their propagation regime inside the interstellar medium changing gradually from diffusive to ballistic as the energy increases.

A pictorial example of how this transition takes place can be seen in figure 6.a-d [41], where it is shown how protons with energies ranging from 0.5 to 6 EeV injected at the Galactic center propagate out of the Galaxy assuming a characteristic BSS magnetic model.

It must be noted that, despite the fact that the deflections induced by the Galactic magnetic field (GMF) diminish rapidly with energy for all nuclei, they can still be important even at the highest energies. This is more critical for heavier primaries and for all nuclei traversing the central regions of the Galaxy. Figure 7 illustrated this point by showing the intrinsic deflections experienced by proton and iron nuclei as a function of arrival Galactic coordinates [42].



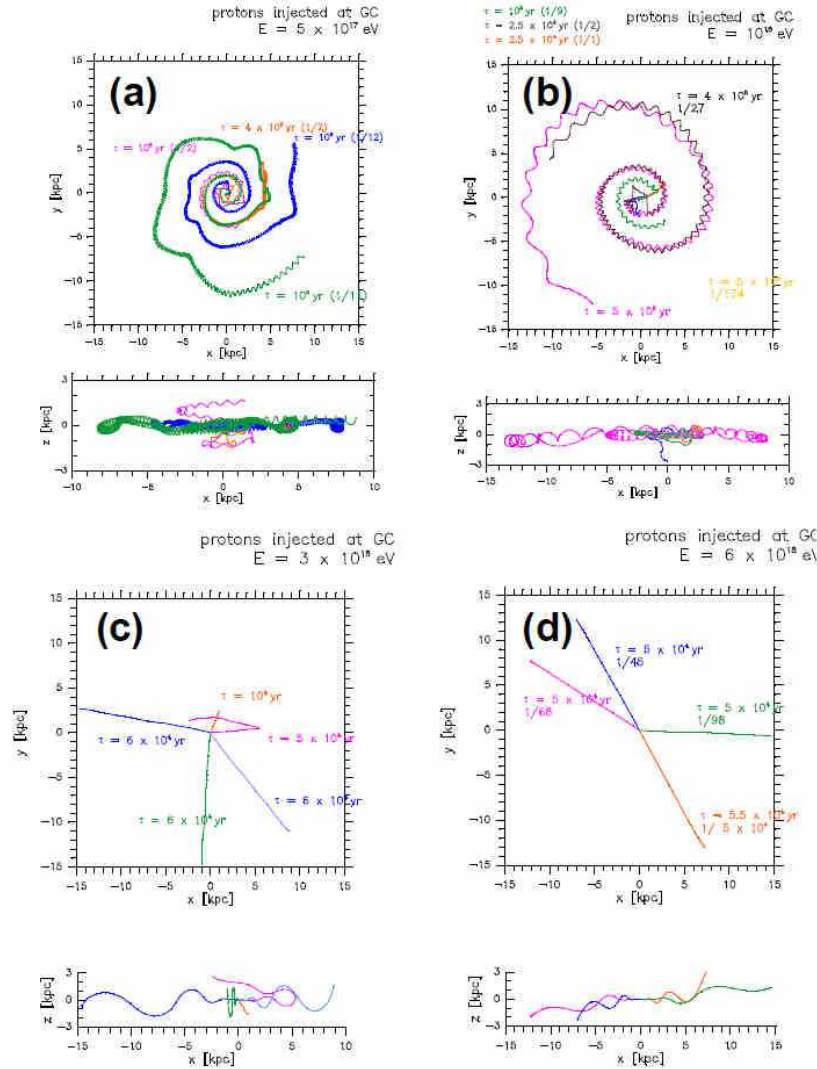


**Fig. 6.** Changes in propagation regime inside the Galaxy at energies of the second knee and ankle.

Figure 8 shows Galactic deflections for 100 EeV protons for a more sophisticated GMF model inspired on Hans proposal [11]. The GMF is modelled by a disk BSSS component of 100 pc half thickness, embedded in an ASSA halo and a dipolar component originated in a Southward magnetic momentum anchored at the Galactic center. Galactic coordinates in an Aitof projection are used.

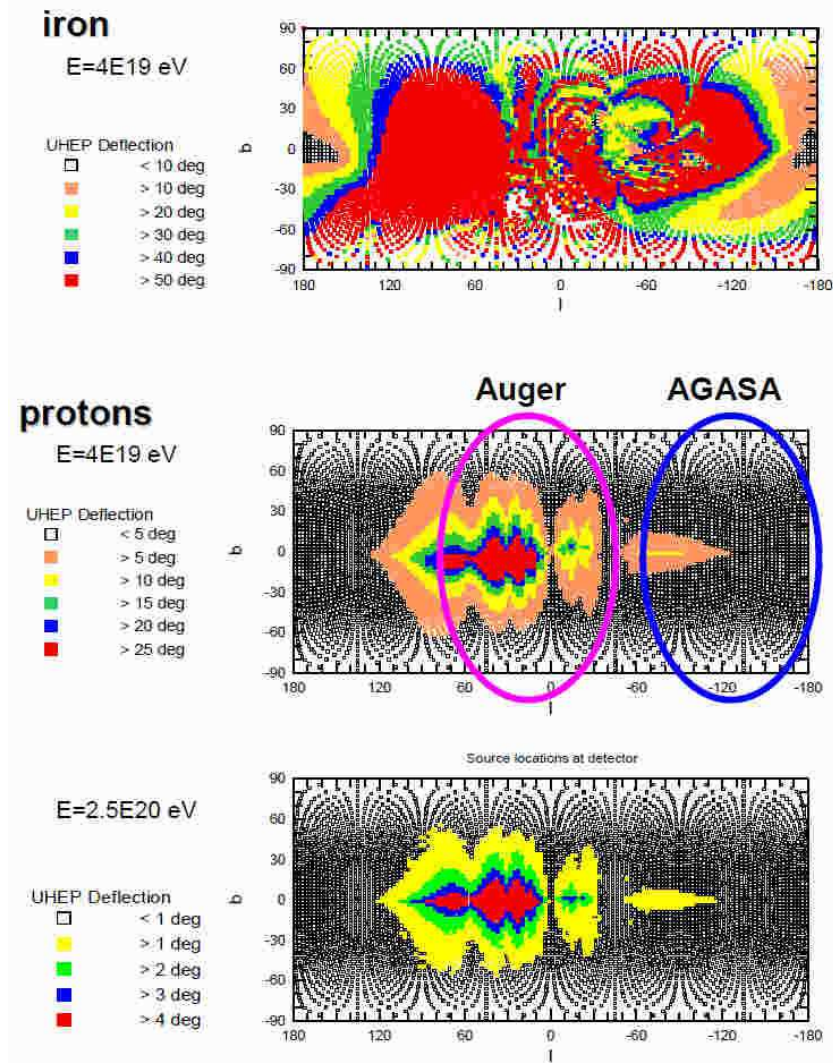


**Fig. 7.** Intrinsic deflections due to the GMF (BSSS model) suffered by protons and Fe nuclei at  $4 \times 10^{19}$  eV and protons at  $2.5 \times 10^{20}$  eV as a function of arrival direction. Galactic coordinates are used.

## 4 Extragalactic propagation

### 4.1 Superposition of the extragalactic and Galactic fluxes

In the same way as the magnetic characteristic of the interstellar medium allow Galactic particles at these energies to escape into the extragalactic environ-

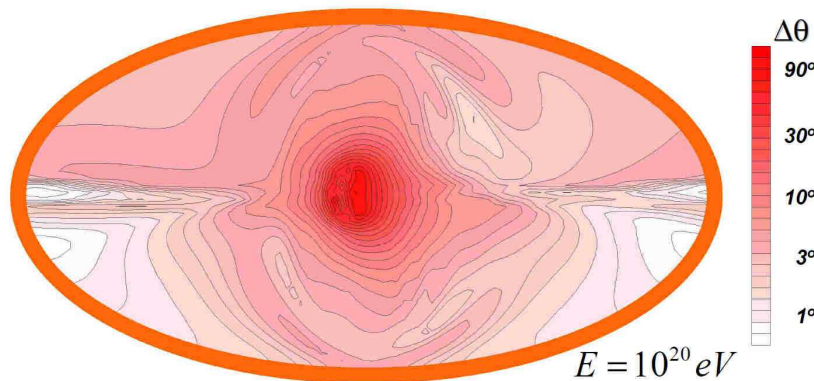


**Fig. 8.** Deflection suffered by 100 EeV protons due to a Han-type GMF (see text) as a function of arrival direction. Galactic coordinates are used in an Aitof projection.

ment, extragalactic cosmic rays are also able to penetrate inside the Galactic confinement region. But, of course, extragalactic particles must first be able to reach us from the nearest Galaxies in less than a Hubble time.

A crude approximation to this effect can be made in the following way.

Faraday rotation measurements statistically impose to the extragalactic magnetic field the following restriction [43]:

$$B \times L_c^{1/2} \leq 1nG \times Mpc^{1/2} \quad (3)$$

where  $L_c$  is the correlation length of the magnetic field that we assume, somewhat arbitrarily, as being of the order of 1 Mpc. Assuming that the diffusion coefficient can be estimated by the Bohm approximation,

$$K \approx \frac{1}{3} r_L c \quad (4)$$

and using equation (1) the diffusion coefficient can be written:

$$K \approx \frac{0.1}{Z} \left( \frac{E_{EeV}}{B_{\mu G}} \right) \frac{Mpc^2}{Myr} \quad (5)$$

The diffusive propagation time from an extragalactic source at a distance  $D$  can be estimated as:

$$\tau \approx \frac{D^2}{K} \quad (6)$$

or, using equation (5):

$$\tau_{Myr} \approx 10 \times D_{Mpc}^2 \times Z \times \left( \frac{B_{nG}}{E_{EeV}} \right) \quad (7)$$

Equation (7) shows that there is a rather restrictive magnetic horizon. Basically, no nucleus with energy smaller than  $10^{17}$  eV is able to arrive from regions external to the local group ( $D \sim 3$  Mpc). Taking as a minimum characteristic distance  $D = 10$  Mpc, which defines a very localized region completely internal to the supergalactic plane and even smaller than the distance to the nearby Virgo cluster, only protons with  $E > 2 \times 10^{17}$  eV, or Fe nuclei with  $E > 5 \times 10^{18}$  eV are able to reach the Galaxy in less than a Hubble time.

Therefore, it is at the energies of the second knee and the ankle that different nuclei start to arrive from the local universe. Concomitantly, at these same energies, the magnetic shielding of the Galaxy becomes permeable to these nuclei, allowing them to get into the interstellar medium and, eventually, to reach the solar system. Effectively, the energy interval from  $\sim 2 \times 10^{17}$  to  $10^{19}$  eV is the region of mixing between the Galactic and extragalactic components of cosmic rays.

Above few times  $10^{17}$  eV, the dominant interactions experienced by cosmic rays are due to the cosmic microwave background radiation (CMBR) and, additionally in the case of nuclei, to the infrared background (CIBR) [44]. The diffuse background in radio, despite its much lower density, must in turn become important at high enough energies.

At energies above  $\sim 10^{19.2}$  eV, the dominant process is the photo production of pions in interactions with the CMBR (see figure 9.a), which drastically reduces the mean free path of protons to a few Mpc, making the universe optically thick to ultra-high energy cosmic rays (9.b). This interaction, in the most conservative models, should produce a strong depression in the energy spectrum, with a major fall in the observed flux above  $10^{20}$  eV, the so called GZK cut-off [46, 47].

At energies smaller than  $\sim 10^{19.2}$  eV, the dominant process is the photo-production of electron-positron pairs in interactions with the CMBR. At these lower energies the attenuation length attain values of the order of Gpc and, therefore, the universe is essentially optically thin to energetic baryons. CR observations at these energies, sample the universe at cosmological distances, contrary to the highest energies, that only sample a sphere of a few tens of Mpc in diameter, a small portion of the local universe [50, 51, 52]. Therefore, strictly from the point of view of propagation in the extragalactic medium, in going down from the highest energies to the transition region, the observable horizon drastically increases from  $10^1$  to  $10^3$  Mpc, i.e., essentially the whole universe.

It can also be seen from figure 9.a that the dependence of the cross section with energy is suggestive, since its shape resembles that of the ankle in the cosmic ray energy spectrum. In fact, the structure of the ankle can be explained exclusively as a result of pair photo-production by nucleons travelling cosmological distances between the source and the observer [48].

The energy region where the superposition of the Galactic and extragalactic spectra takes place is a theoretically challenging region, where the smooth matching of the two rapidly varying spectra has yet to be explained. It must

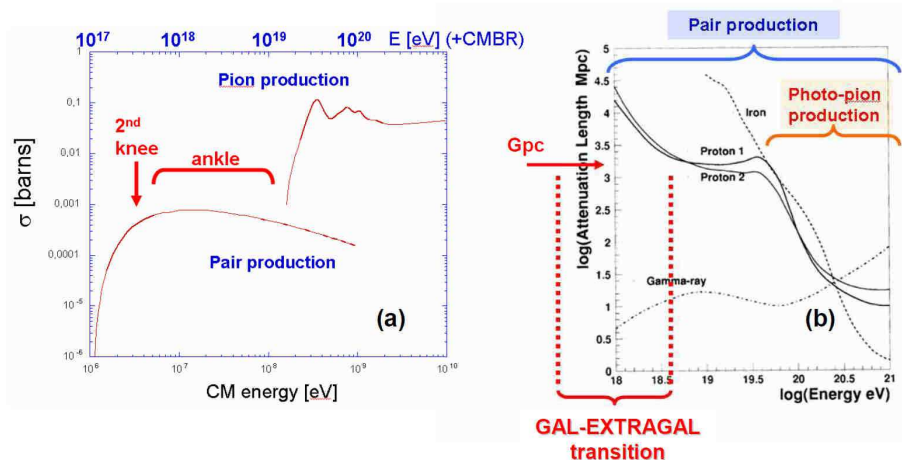


**Fig. 9.** (a) Cross section for pair production and pion production in interaction with the CMBR. The positions of the second knee and the ankle are also shown, demonstrating that electron positron pair production is the relevant interaction in the Galactic-extragalactic transition region. Note the similitude between the shape of the cross section for this interaction and the shape and location of the ankle. (b) Attenuation length in Mpc as a function of energy [45], showing how the universe, which is opaque for at energies above the photo-pion production threshold, becomes transparent to lower energy barions.

be noted that, even if the shape of the spectrum is important, it is by far insufficient to decipher the underlying astrophysical model. The Galactic magnetic fields are intense enough to dilute any directional information, which prevents the discrimination among the galactic and extragalactic components from the arrival direction of the incoming particles. The variation of the composition as a function of energy turns then into the key to discriminate both fluxes and to select among a variety of theoretical options.

As in the case of the interstellar medium, it is expected that the intergalactic medium has a strong magnetic turbulent component which can severely affect propagation [53, 54, 55, 56, 57, 58]. The correlation length estimated from Faraday rotation measurements,  $L_c$ , is consistent with a maximum wavelength for the MHD turbulence determined by the largest kinetic energy injection scales in the intergalactic medium,  $L_{max} \sim L_c \sim 1$  Mpc. Therefore, analogous to equation (2):

$$r_{L,kpc} \approx \frac{1}{Z} \times \left( \frac{E_{EeV}}{B_{nG}} \right) \approx L_{max} \quad , \quad L_{max} \approx 1Mpc \quad \Rightarrow \quad E_{c,EeV} \approx 1.0 \times Z \quad (8)$$

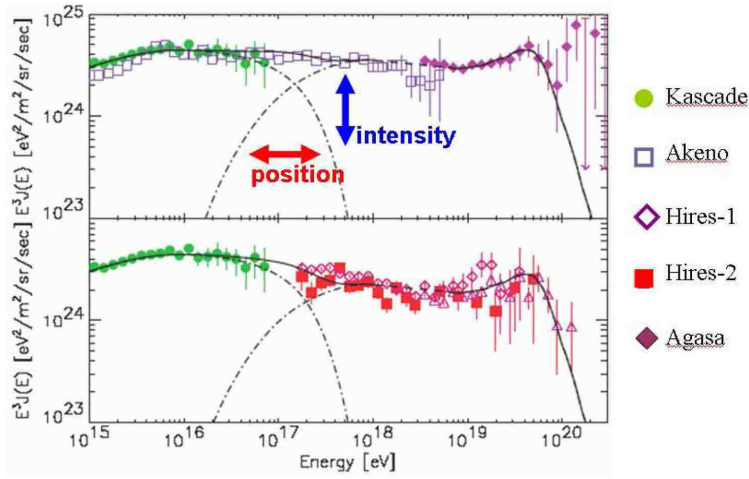


**Fig. 10.** Total cosmic ray spectrum from the combined data of several experiments. From the theoretical point of view, the transition region is highly complex and the Galactic and extragalactic models suffer their most critical test since the corresponding fluxes must be simultaneously matched both in intensity and energy. (Adapted from: [49].)

For a given nucleus of charge  $Ze$ , the propagation is ballistic for  $E > E_c$  being diffusive otherwise. Therefore, protons are ballistic above  $\sim 10^{18}$  eV, but diffusive at the energies of the second knee. Iron nuclei, on the other hand, propagate diffusively along the ankle and even at energies as high as  $\sim 5 \times 10^{19}$  eV. The boundaries for the transition between the ballistic and diffusive propagation regime for proton and Fe nuclei are shown in the figure 11.

Furthermore, besides the total intensity and the minimum wavenumber, also the energy distribution among the different modes, that is the type of turbulence present in the intergalactic medium, have observational expression. In this case, the affected portion of the extragalactic spectrum is the region of lower energies, where the flux is strongly suppressed by magnetic horizon effects. Figure 11 shows clearly this effect for three different assumptions for the diffusion coefficient.

Obviously, this has profound theoretical implications not only for the structure of the extragalactic magnetized medium, but also for cosmic ray acceleration conditions inside the Galaxy. This is exemplified in figure 12 where it is graphically illustrated that, by subtracting a given extragalactic spectrum from the observed total spectrum, conclusions can be drawn about relevant aspects of the Galactic component. For example, an extragalactic spectrum that has a small contribution at low energies, can imply the existence of ad-

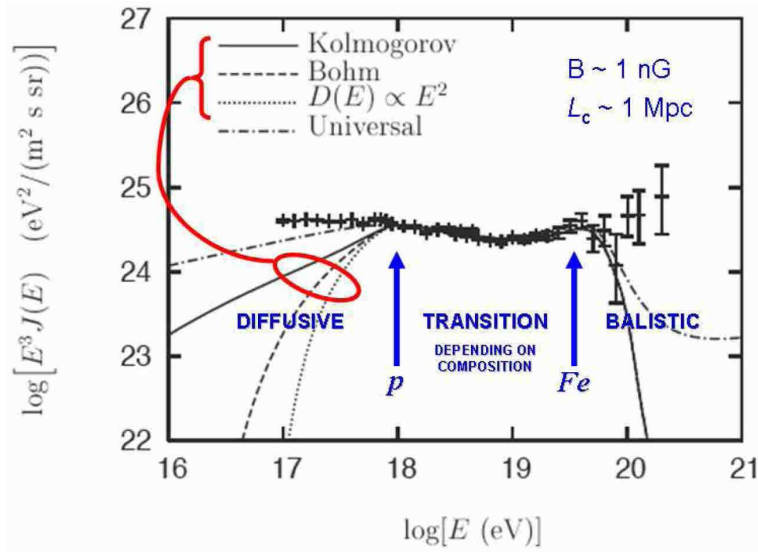


**Fig. 11.** Correlation between the detailed structure of the lower end of the extragalactic spectrum and the type of turbulence present in the intergalactic medium. This emphasizes the importance of the intergalactic turbulent component in the observed matching between the Galactic and extragalactic cosmic ray flux. (Adapted from: [59].)

ditional acceleration mechanisms in the Galaxy other than the shock waves of supernova remnants.

## 4.2 The highest energies

### Propagation of protons

As was mentioned in the previous section 4.1 (see figure 9), above the threshold for photo-pion production by protons interacting with the CMBR,  $\sim 40$  EeV the universe becomes rapidly opaque for hadrons as the attenuation length goes down to values as low as  $\sim 10$  Mpc at  $\text{few} \times 10^{20}$  eV. This determines a relatively small (in cosmological terms) maximum distance scale,  $R_{GZK} \simeq 50\text{--}100$  Mpc, to the sources that are able to contribute appreciably to the detected CR flux.

Under very general assumptions regarding the nature of the primaries and the cosmological distribution of the sources, photo-pion production should lead to the formation of a pile-up immediately followed by a severe reduction in CR flux, popularly known as the GZK cut-off. The existence of this spectral feature was proposed short time after the discovery of the CMBR [46, 47] but its actual existence is still a matter of considerable debate.

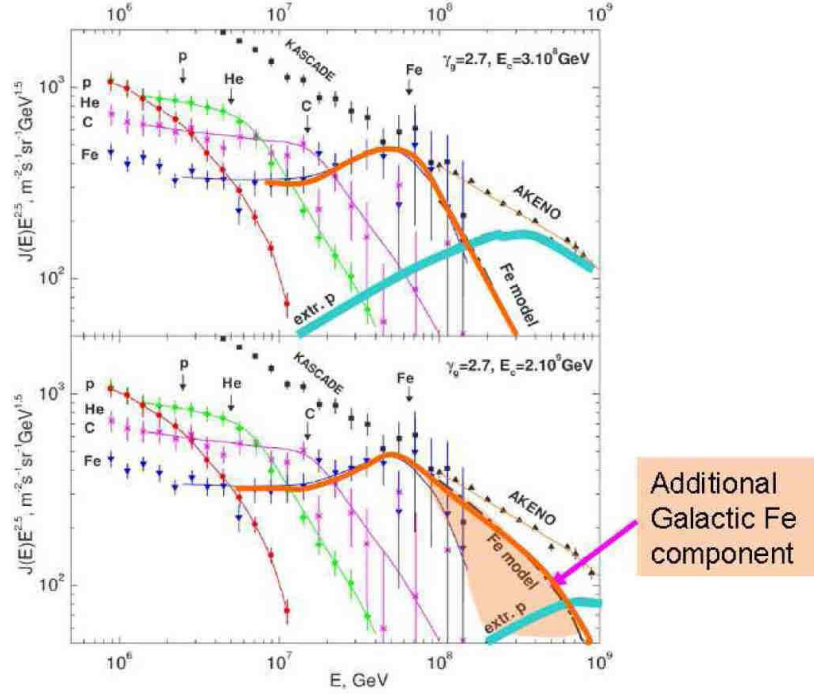


**Fig. 12.** Impact of the detailed characteristics of the extragalactic spectrum on our comprehension of the most powerful acceleration mechanisms in our Galaxy. (Adapted from: [60].)

At present, there are conflicting measurements coming from two different experiments: AGASA and HiRes. The first one is a surface detector while the second one is a fluorescence detector, which further complicates the comparison of their results.

As shown in figure 13, the differences are not only quantitative but, fundamentally, qualitative. While HiRes apparently shows the expected GZK flux suppression, AGASA seems incompatible with this result, showing an energy spectrum that extends undisturbed well beyond 100 EeV. There is also an apparently large difference in flux between both experiments at energies below the cut-off. However, the fact that the energy spectrum has been multiplied by  $E^3$  in figure 13 should be taken into account when assessing the significance of such difference.

Actually, both results might be reconciled at the  $1.5\sigma$  level by re-scaling the energy of either of the experiments by 30% or by 15 % each [62]. The Auger Observatory, being the largest detector ever built and having hybrid capacity (i.e., simultaneous fluorescence and surface detection [63]) has the



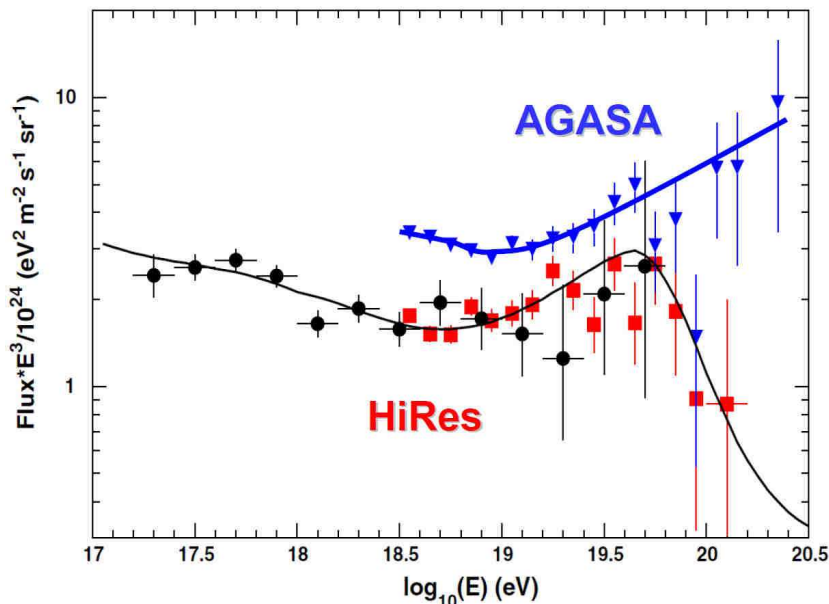


**Fig. 13.** Comparison between the AGASA and Hires monocular spectra. (Adapted from: [61].)

potential, but not enough statistics at present, to give a definite answer to this fundamental problem [64].

The absence of the GZK cut-off, if confirmed, could be compatible with a wide range of astrophysical scenarios. At least three possibilities can be considered, some rather conservative, some more exotic:

- The distance scale between sources could be large enough that, by chance, the few (or single) sources inside the GZK sphere dominate the flux, the rest of the population of UHECR accelerators being too distant to contribute appreciably to the observed flux at Earth.
- The primary CR might be particles that do not interact with photons or do so at much larger, and as yet unobserved, energies. These could be familiar standard model particles that present unexpected behavior at ultra-high energies, like neutrinos with hadronic cross section that can develop showers in the atmosphere resembling those expected from proton primaries [65, 66]. Another possibility could be a new stable hadron, heavier than a nucleon, for which the threshold for photo-meson production would be at higher energy. An example of the latter would be uhechons, e.g., a uds-gluino bound state [67].
- The primaries might be normal hadrons, but Lorentz invariance, which has never been previously tested at  $\gamma \sim 10^{11}$ , could be violated at ultra-

high energies, hampering photo-meson production [68, 69, 70]. The small violation of Lorentz invariance required might be the result of Planck scale effects [71, 72].

- The observed spectrum could be the superposition of two components: (a) a hadronic component with a GZK cut-off and (b) a harder, top-down component that becomes dominant above  $\sim 100$  EeV. These second component could be originated in the decay or annihilation of super heavy dark matter or topological defects [73, 74, 75, 77]. These scenarios have the general disadvantage of overproducing ultra-high energy neutrinos and photons rather than nucleons, which seems to be increasingly constrained by the observation [34, 82]. Nevertheless, there could still be models, like those involving necklaces, that could present an appreciable baryon content at energies  $\gtrsim 100$  EeV [76]. In any case, these models suffer from a discomforting level of fine tuning with respect to the normalization of the intensities of the GZKed and the top-down spectra.

It must also be noted that the presence of the GZK flux suppression does not imply the non-existence of supra-GZK particles in the CR flux. These have certainly been detected by at least Volcano Ranch [78, 79], Flys Eye [80], AGASA, HiRes and, more recently, Auger [81]. This means that, the detection of the GZK feature does not solve the puzzle about the generation of UHECR.

### Propagation of UHE photons

The propagation of photons is dominated by their interaction with the photon background. The main processes are photon absorption by pair-production on background photons ( $\gamma\gamma_b \rightarrow e^+e^-$ ), and inverse Compton scattering of the resultant electrons on the background photons. These two processes acting in a chain are responsible for the rapid development of electromagnetic cascades in the intergalactic or interstellar media, draining energy to the sub-TeV region.

For a given UHE photon of energy  $E_\gamma$ , the minimum background photon energy,  $E_b$ , for electron-positron pair production is:

$$E_b = \frac{m_e^2}{E_\gamma} \simeq \frac{2.6 \times 10^{11}}{E_{\gamma,eV}} \text{ eV} \quad (9)$$

and the corresponding cross section peaks near the threshold:  $\sigma_{PP} \propto (m_e^2/s) * \ln(s/2m_e)$ . Inverse Compton scattering, on the other hand, has no threshold but its cross section is also largest near the  $\gamma\gamma_b$  pair production threshold. Therefore, the most efficient background for both processes is given by equation (9). For UHE this means that the cosmic radio background, whose magnitude is highly uncertain, is dominant followed by the CMBR below  $10^{17}$  -  $10^{18}$  eV. At progressively lower energies, the CIRB and optical background are important.

In the Klein-Nishina limit,  $s \gg m_e^2$ , one of the components of the  $\gamma\gamma_b$ -produced pair carries most of the energy of the UHE photon. This leading particle, afterwards, undergoes Compton scattering in the same limit, for which the inelasticity is very near 1. Therefore, the Compton up-scattered photon still has an appreciable fraction of the energy of the original UHE photon. The presence of magnetic fields in the medium may speed up the development of the cascade by draining the electron and positron energy due to synchrotron radiation. The larger the fields, the smaller the penetration.

The electromagnetic cascades produced in this way can propagate an effective distance that is much larger than the interaction length yet, severely limit our UHE- $\gamma$  horizon to the nearest regions of the supergalactic plane. Figure 14 [73] shows the effective penetration length of electromagnetic cascades for two different estimates of the cosmic radio background and two different average intergalactic magnetic field intensities.

Since the single pair cross section decreases as  $\ln(s)/s$  for  $s \gg m_e^2$ , multiple pair production becomes important at extreme energies. Thus, double pair production ( $\gamma\gamma_b \rightarrow e^+e^-e^+e^-$ ) begins to dominate above  $\sim 10^{21} - 10^{23}$  eV. The relevant process for electrons is triple pair production ( $e^\pm\gamma_b \rightarrow e^\pm e^-e^+$ ), whose attenuation becomes dominant at  $\sim 10^{22}$  eV. Other processes (e.g., muon, tau or pion pair production, double Compton scattering, gamma scattering and pair production of single photons in magnetic fields) are in general negligible for electromagnetic cascade development. However, at energies in excess of  $10^{24}$  eV, the pair production of single photons in the Galactic magnetic field should eliminate all the photons above that energy from specific lines of sight, generating an arrival direction anisotropy.

The penetration lengths shown in figure 14, combined with the threshold energies given by equation (9), imply that the injection of UHE- $\gamma$  in the intergalactic medium results in the pile-up of photons at energies below 100 MeV, whose contribution to the diffuse cosmic  $\gamma$  background is already observationally constrained by EGRET. This overproduction of low energy diffuse photons is a strong restriction for top-down UHECR production models.

Besides the limitations imposed by the possible overproduction of low energy photons, the results in figure 14 have other profound implications for top-down scenarios. Models that claim decay or annihilation of DM, in general, tend to produce mainly photons and only a few percent baryons. Therefore, in such models, most of the detected CR should be photons from our own Galactic halo, with perhaps some localized contribution from Andromeda. The products of the decay of more distant dark matter would be cleared from photons, and only the small fraction of remaining baryons, suppressed by GZK effects, would give a positive contribution at Earth. In any case, for most top-down models, photons should be dominant above the GZK cut-off, but with perhaps a sizable baryonic component.

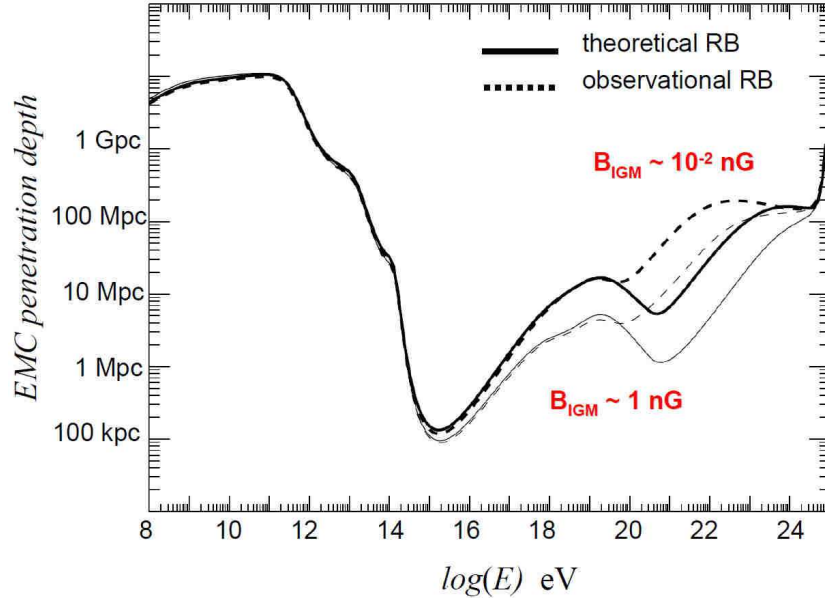


**Fig. 14.** Penetration of electromagnetic cascades in the intergalactic medium. Solid lines correspond to a fiduciary value of 1 nG for the IGMF and dotted lines to a very low IGMF,  $10^{-2}$  nG. Thick and thin lines correspond to different estimates of the cosmic radio background. (Adapted from: [73].)

### Propagation of nuclei

Heavy nuclei are attenuated by basically two processes: photodisintegration and electron-positron pair creation by interaction with background photons.

For the same total energy, the threshold photo-pion production for a nucleus of mass  $A$  increases to  $E_{th} \simeq 4 \times 10^{19} \times A$ . Therefore, given the energies observed at present, pion production is not relevant for nuclei heavier than He.

Figure 15 shows that below  $\sim 20$  EeV, all nuclei are able to travel for virtually a Hubble time, while Fe can do the same up to  $\sim 100$  EeV. Above that energy, nuclei start to disintegrate fast and the loss time is highly reduced.

It is clear from composition observations around the first knee of the cosmic rays spectrum that the acceleration mechanism by shock waves, either first order Fermi or drift are limited by the magnitude of the radius of curvature of the shock. This results in the preferential acceleration of large charge ( $eZ$ ) nuclei, those with the smallest Larmor radius, to the highest energies.

Even if the mechanism responsible for the acceleration of the ultra-high energy extragalactic component is essentially unknown, the most conservative

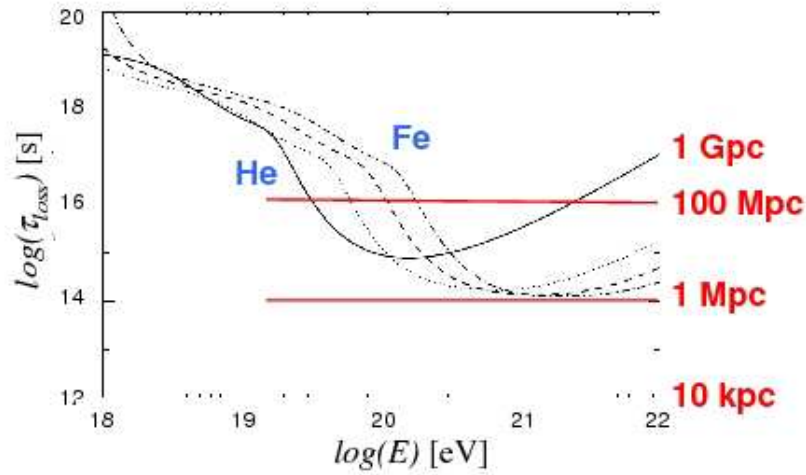


**Fig. 15.** Energy loss time (right axis: length) vs. energy for photodisintegration on background photons: radio, CMB and IR. Helium, Carbon, Silicon and Iron are shown. Single, double and multi-nucleon emissions are included. (Adapted from: [83].)

view points to bottom-up mechanisms. If the later is actually the case, then the most economic assumption is that chock wave acceleration.

In this minimalistic, but still realistic, scenario the most likely high energy output would be heavy nuclei, very likely Fe as in the Galactic case. At lower energies, progressively lighter nuclei should be observed due to two factors: (a) the acceleration process in itself and (b) the photo-disintegration on flight of the heavier nuclei due to their interaction with the CIBR. The latter process is very efficient, and can extract approximately one nucleon every few Mpc at the highest energies, depending on the CIBR level. Since photodisintegration occurs, to a good approximation, at constant energy per nucleon, disintegration of a nucleus  $A$  at energy  $E$  will produce light nuclei at energies  $nE/A$  and  $(A - n)E/A$  with preferentially small  $n$  (e.g.,  $n = 1, 2, 3, 4$ ).

Figure 16 shows that power law spectra injected at cosmological sources with different compositions can produce experimentally very similar at the highest energies. Nevertheless, they can always be distinguished at smaller energies in the ankle region.

In particular, figure 16.a showshow a purely protonic flux can reproduce the ankle feature solely as an effect of photo production of electron-positron pairs in interactions with the CMBR. In this case, the transition between the Galactic and extragalactic fluxes must be located at the second knee or very near to it.

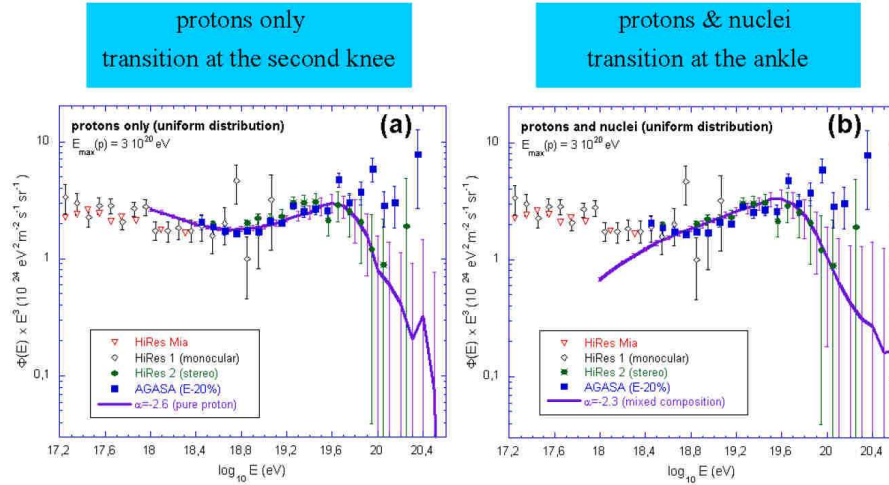


**Fig. 16.** Different primary compositions may produce extragalactic spectra essentially indistinguishable at the highest energies. However, as shown in (a) for protons and (b) for heavier mix, the spectra are considerably different at lower energies below the bottom of the ankle. (Adapted from: [84].)

Figure figure 16.b, on the other hand, shows that, for a heavier mixed composition, the extragalactic spectrum falls down steadily with decreasing energy. In this scenario, the ankle must be the result of the composition between the Galactic and extragalactic spectra. Moreover, the composition will be a strong function of energy inside this interval, giving an additional tool to assess details of the astrophysical model.

The effects of photo-disintegration are clearly shown in figure [85], where the evolution of a pure iron injected spectrum as it propagates out from the source. Blue histograms correspond to p, white to the original surviving Fe and red to intermediate mass nuclei.

As the distance to the source increases, intermediate nuclei are produced at increasingly smaller masses and less total energy (fragmentation takes place at roughly constant mass per nucleon). At distances of the order of the GZK horizon, the region with larger mixing of nuclei, i.e., with a larger composition gradient, is the ankle. Consequently, this is the ideal region for the discrimination of the primary composition from local composition measurements.

## 5 Cosmic magnetic fields and anisotropy

Luminous matter, as traced by galaxies, as well as dark matter, as traced by galaxies and clusters large scale velocity fields, is distributed inhomogeneously in the universe. Groups, clusters, superclusters, walls, filaments and voids are

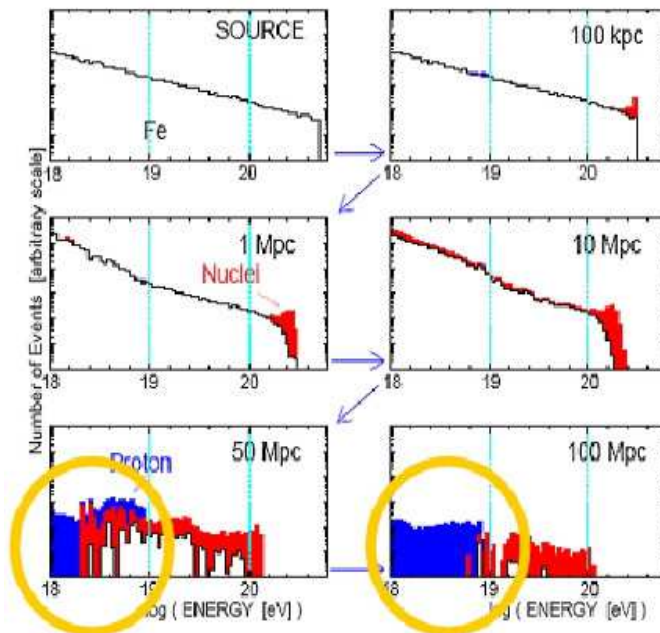


**Fig. 17.** Variation of the composition as a function of distance to the source for pure Fe power law injection. Blue histograms correspond to p, white to the original surviving Fe and red to intermediate mass nuclei. (Adapted from: [85].)

known to exist at all observed distances and are very well mapped in the local universe. Hence, the distribution of matter inside the GZK-sphere is highly inhomogeneous and so is, very likely, the distribution of UHECR sources.

Synchrotron emission and multi-wavelength radio polarization measurements show that magnetic fields are widespread in the Universe. But how do they encompass the structure seen in the distribution of matter we do not yet know [43].

The available limits on the IGMF come from rotation measurements in clusters of galaxies and suggest that  $B_{IGM} \times L_c^{1/2} < 10^{-9} \text{ G} \times \text{Mpc}^{1/2}$  [43], where  $L_c$  is the field reversal scale. Note, however, that this kind of measurement doesn't set an actual limit to the intensity of the magnetic field unless the reversal scale is known along a particular line of sight. The latter means that, depending on the structure of the IGMF, substantially different scenarios can be envisioned that are able to satisfy the rotation measurement constraints.

Unfortunately, we do not know what is the actual large scale structure of the IGMF. Nevertheless, we can imagine two extreme scenarios that are likely to bound the true IGMF structure. In figure 18 calculations of large

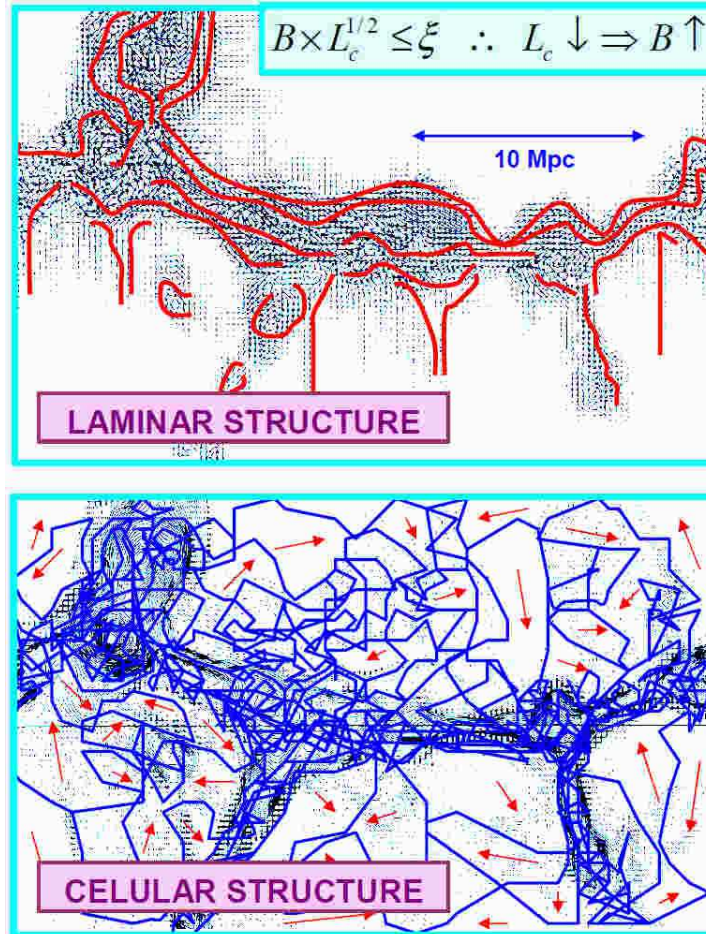


**Fig. 18.** two possible extreme models for the IGMF structure: (top) laminar structure and (bottom) cellular structure. These schematic plots are adaptations by hand made on top of IGMF and density calculations by [100]

scale structure formation by Ryu and co-workers [100] have been modified by hand to exemplify these scenarios. The top frame displays Ryu's IGMF simulation results in the background showing how, by  $z = 0$ , the magnetic field has been convected together with the accretion flows into walls, filaments and clusters, depleting the voids from field. According to these calculations, the magnetic field is confined in high density, small filling factor regions, bounded by a rather thin skin of rapidly decreasing intensity, surrounded by large volumes of negligible IGMF. As suggested by the free-hand lines on top of the figure, the IGMF inside structures is highly correlated in scales of up to tens



of Mpc. Furthermore, in order to comply with the rotation measurement constraints mentioned before, the intensity of the magnetic field inside the density structures must be correspondingly high,  $0.1\text{--}1\ \mu\text{G}$ , which is comparable with GMF values within the interstellar medium. We will call the latter scenario *laminar-structure*.

The second model, that we will call *cellular-structure*, is depicted in the bottom panel of figure 18. We imagine the space divide into adjacent cells, each one with a uniform magnetic field randomly oriented. We identify the size of a cell with the magnitude of the local reversal scale. Furthermore, one can assume that the intensity of the magnetic field scales as some power of the local matter (electron) density and, consequently, the rotation measurement constraint  $B_{IGM} \times L_c^{1/2} < 10^{-9}\ \text{G} \times \text{Mpc}^{1/2}$  tells how the reversal scale, i.e., the size of the cells, should be scaled. A convenient reference, such as the IGMF in the Virgo [86] or Coma [90] cluster can be used for normalization. The cellular-structure scenario leads to a more widespread IGMF, filling even the voids. The observational constraints imply then that the IGMF varies much more smoothly, from  $10^{-10}\text{G}$  inside voids to a few times  $10^{-9}\text{--}10^{-8}\text{G}$  inside walls and filaments, only reaching high values,  $0.1\text{--}1\ \mu\text{G}$ , inside and around clusters of galaxies.

Observations are not enough at present to distinguish between these two scenarios. Nevertheless, we can still try to asses what are their implications for UHECR propagation which, inspecting figure 19, must be important.

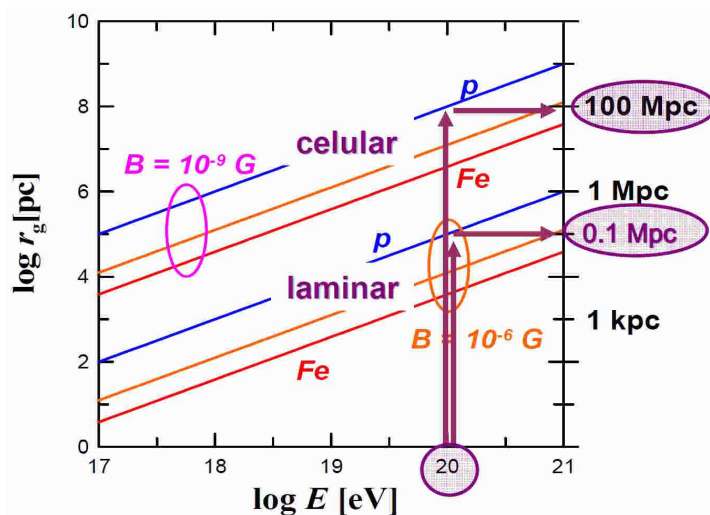


**Fig. 19.** Typical Larmor radii of nuclei in both IGMF scenarios, showing the very different scales involved in each model.

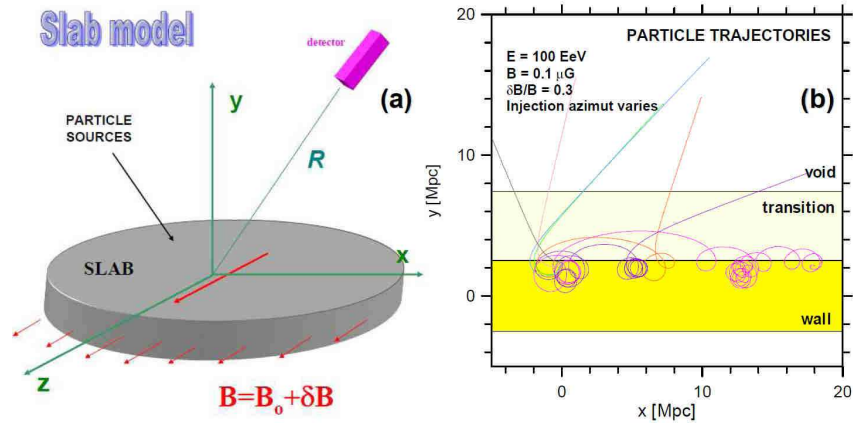


**Fig. 20.** (a) Simplified model of a wall, or slab, containing UHECR sources and surrounded by a void. The magnetic field configuration is representative of the laminar model. (b) Cross section of the wall in (a) at the plane  $z = 0$ . Several particles trajectories are shown for proton injection at  $E = 100 \text{ EeV}$ . Adapted from [94].

### 5.1 UHECR propagation in a laminar-IGMF

This is the most difficult scenario to deal with because it does not accept a statistical treatment and results are very dependent on details about the exact magnetic field configuration inside the GZK-sphere, which is beyond our present knowledge.

A simpler approach is to study the UHECR emissivity of a single wall surrounded by a void [95, 94]. Figure 20.a shows the corresponding model for a wall immersed in a void; the magnetic field inside the wall has two components, a uniform field along the  $z$ -axis of intensity  $0.1 \mu\text{G}$  and a random component with a Kolmogoroff power law spectrum of amplitude equal to 30% of the regular component. One hundred UHECR sources are included inside the wall, and each one of them injects protons at the same rate and with the same power law energy spectrum,  $dN_{inj}/dE \propto E^{-2}$ . Pair-production and photo-pion production losses in interactions with the infrared and microwave backgrounds respectively are also included. The wall has a radius of 20 Mpc, a thickness of 5 Mpc and is sandwiched by a transition layer 5 Mpc in thickness where the magnetic field decreases exponentially up to negligible values inside the surrounding void. Once the system reaches steady state, a detector can be shifted around the wall to simulate observers at arbitrary positions with respect to the wall. In a real situation, this system could be representative, for example, of the supergalactic plane; in that case the Milky Way, i.e. we, the observers, should be located at some point on the  $x$ - $z$  plane (but we don't know at what angle with respect to the  $z$ -axis). The simulations show that the UHECR flux measured can vary by three orders of magnitude depending

of the relative orientation between the wall, the field and the observer. At the same time, almost all directional information is lost, and the strength of the GZK-cut-off would vary considerably as a function of orientation [94].

The previous effects can be intuitively understood by looking at figure 20.b, which shows a cross section of the wall in figure 20.a at the plane  $z = 0$ . Several particles trajectories are shown for proton injection at  $E = 100$  EeV, with different azimuthal angles and a slight elevation with respect to the  $x$ - $y$  plane. It can be seen that there is nothing like a random walk: particles tend to be trapped inside the wall and move in a systematic way. Most of the particles drift perpendicularly to the regular field while their guiding centers bounce along the field. It can also be seen how the gyroradii decrease as the particles lose energy in interactions with the radiation backgrounds. Even the few particles that do escape from the wall, do so in a non-isotropic manner (e.g., predominantly to the right for  $y > 0$ ).

The laminar IGMF model is, actually, the worst scenario for doing some kind of astronomy with UHECR. It would be very difficult to interpret the UHECR angular data and to identify individual particle sources. Furthermore, the significance of any statistical analysis would be greatly impaired due to systematics.

Further studies on this model can also be found, for example, in references [104, 105].

## 5.2 UHECR propagation in a cellular-IGMF

The cellular model is the easiest scenario to deal with numerically and, by far, the most promising from the point of view of the astrophysics of UHECR. This is also the IGMF model that has been used probably more frequently in the literature [87, 91, 54, 92, 93, 96, 98, 99].

The main assumption here, is that the intensity of the magnetic field scales with density. Indeed, for those spatial scales where measurements are available, the intensity of the magnetic fields seem to correlate remarkably well with the density of thermal gas in the medium. This is valid at least at galactic and smaller scales [101, 97]. It is apparent that  $B$  can be reasonably well fitted by a single power law over  $\sim 14$  orders of magnitude in thermal gas density at sub-galactic scales. A power law correlation, though with a different power law index, is also suggested at very large scales (c.f. figure 5 in Medina Tanco 2000b), from galactic halos to the environments outside galaxy clusters, over  $\sim 4$  orders of magnitude in thermal gas density. This view [101] is, however, still controversial [43]. In fact, magnetic fields in galaxy clusters are roughly  $\sim 1 \mu\text{G}$ , which is of the order of interstellar magnetic fields; furthermore, supracluster emission around the Coma cluster suggests  $\mu\text{G}$  fields in extended regions beyond cluster cores. The latter could indicate that the IGMF cares little about the density of the associated thermal gas density, having everywhere an intensity close to the microwave background-equivalent magnetic field strength,  $B_{BGE} \simeq 3 \times 10^{-6}$  G.

Taking the view that a power law scaling exist, a model can be devised in which the IGMF correlates with the distribution of matter as traced, for example, by the distribution of galaxies. A high degree of non-homogeneity should then be expected, with relatively high values of  $B_{IGMF}$  over small regions ( $< 1$  Mpc) of high matter density. These systems should be immersed in vast low density/low  $B_{IGMF}$  regions with  $B_{IGMF} < 10^{-9}$  G. Furthermore, in accordance with rotation measurements, the topology of the field should be such that it is structured coherently on scales of the order of the correlation length  $L_c$  which, in turn, scales with IGMF intensity:  $L_c \propto B_{IGMF}^{-2}(r)$ .  $B_{IGMF}$  should be independently oriented at distances  $> L_c$ . Therefore, a 3D ensemble of cells can be constructed, with cell size given by the correlation length,  $L_c$ , and such that:  $L_c \propto B_{IGMF}^{-2}(r)$ , while  $B_{IGMF} \propto \rho_{gal}^{0.35}(r)$  [101] or  $\propto \rho_{gal}^{2/3}(r)$  (for frozen-in field compression), where  $\rho_{gal}$  is the galaxy density, and the IGMF is uniform inside cells of size  $L_c$  and randomly oriented with respect to adjacent cells [92, 99]. The observed IGMF value at some given point, like the Virgo cluster, can be used as the normalization condition for the magnetic field intensity. The density of galaxies,  $\rho_{gal}$ , is estimated using either redshift catalogs [like the CfA Redshift Catalogue [93, 96] or the PSCz [89]], or large scale structure formation simulations [99]. The latter is a convenient way to cope with, or at least to assess the importance of, the several biases involved in the use of galaxy redshift surveys to sample the true spatial distribution of matter in 3D space.

The relevant energy losses for UHECR during propagation are: pair production via  $\gamma-\gamma$  with CMB for photons, redshift, pair production and photopion production in interactions with the CMB for nuclei and, for heavy nuclei, also photo-disintegration in interactions with the infrared background. All of these can be appropriately included [88, 102, 103, 73].

The spatial distribution of the sources of UHECR is tightly linked to the nature of the main particle acceleration/production mechanism involved. However, in most models, particles will either be accelerated at astrophysical sites that are related to baryonic matter, or produced via decay of dark matter particles. In both cases the distribution of galaxies (luminous matter) should be an acceptable, if certainly not optimal, tracer of the sources.

Once the previously described scenario is built, test particles can be injected at the sources and propagated through the intergalactic medium and intervening IGMF to the detector at Earth.

Figure 21a-b show the arrival probability distribution of UHECR protons as a function of galactic coordinates for a distribution of sources following the distribution of luminous matter inside 100 Mpc(CfA2 catalog). A power law injection energy spectrum at the sources is assumed,  $dN_{inj}/dE \propto E^{-2}$ , with (a)  $E_{inj} > 4 \times 10^{19}$  eV and (b)  $E_{inj} > 10^{20}$  eV respectively.

It can be seen that, in contrast to the laminar IGMF case, in this scenario information regarding the large scale distribution of the sources inside the GZK-sphere can be easily recoverable. The supergalactic plane and the Virgo

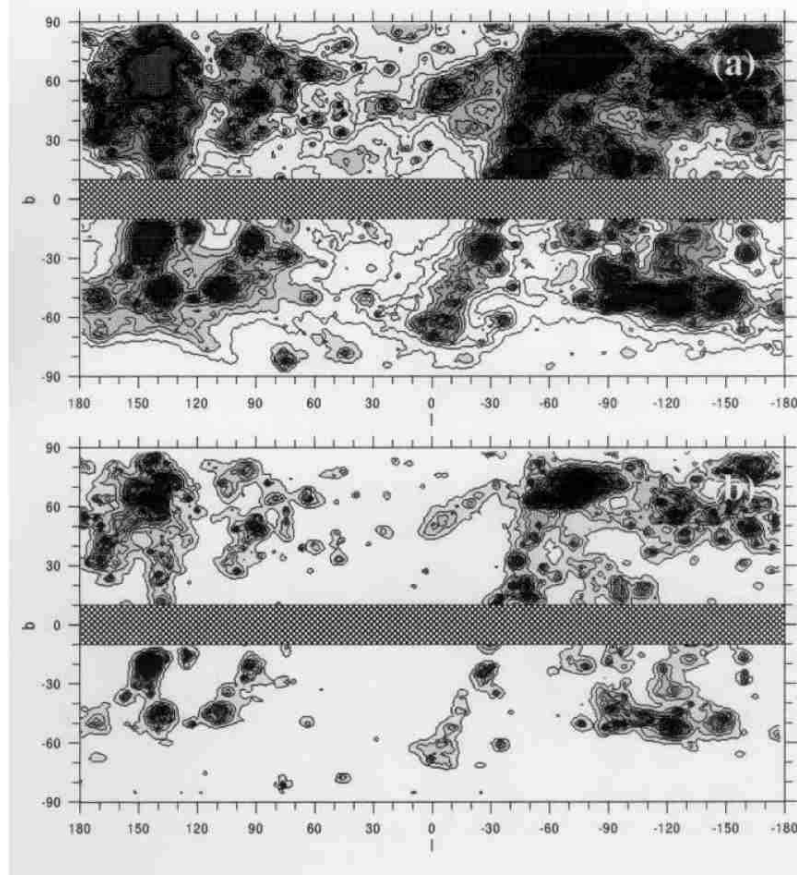


**Fig. 21.** Arrival probability distribution of protons (linear scale) as a function of galactic coordinates for a distribution of sources following the distribution of luminous matter inside 100 Mpc.  $dN_{inj}/dE \propto E^{-2}$ , with (a)  $E_{inj} > 4 \times 10^{19}$  eV and (b)  $E_{inj} > 10^{20}$  eV.

cluster, in particular, are clearly visible between  $l \simeq 0--100$ . It can also be appreciated the increase in resolution as the energy reaches the 100 EeV range and the gyroradii of UHECR protons become comparable to the size of the GZK-sphere. It is also in the cellular model that the deflection angle of the incoming particle with respect to the true angular position of the source (see figure 22) is small enough for an UHECR astronomy to develop at the largest energies.

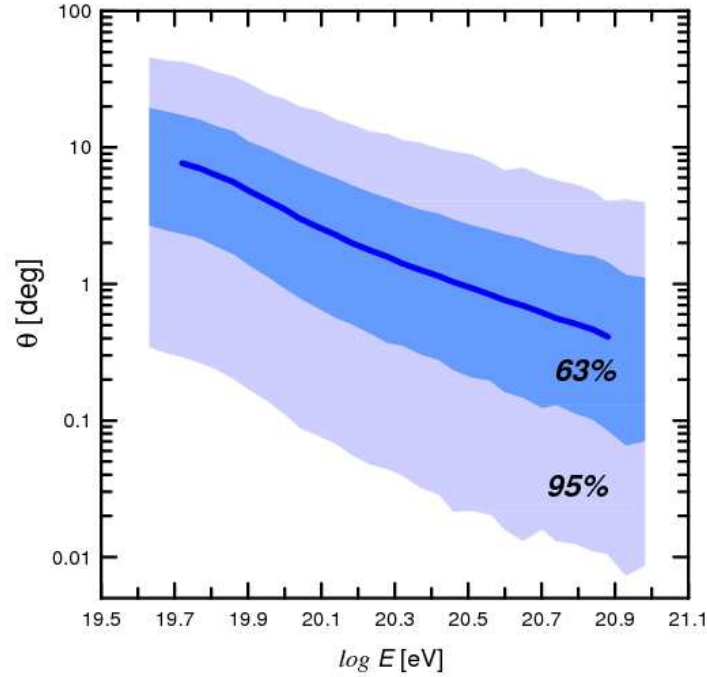


**Fig. 22.** Median and 63% and 95% C.L. for the deflection angle of an incoming UHECR proton with respect to the true angular position of the source for the example in figure 21. All sky average.

### 5.3 Anisotropy observations and magnetic fields

CR anisotropies can be divided, in principle, according to the angular scales they affect at a given energy region: (a) large scales, extending across several tens of degrees in the sky, (b) medium scales,  $\lesssim 10^\circ$  and (c) small scales, of the order of the angular resolution of the experiment, i.e.,  $\sim 1 - 3^\circ$ .

At all energies CR are remarkably isotropic. At energies below  $\sim 100$  TeV, a first harmonic analysis shows an anisotropy amounting to less than 0.07 %. At large energies, on the other hand, measurements are increasingly difficult due to lowering statistics and ambiguities in the interpretation of the data due to the non-uniformity of the detectors acceptance [106, 107]. Nevertheless, all the data available is consistent with large scale isotropy [108, 109, ?, 81].

In fact, besides the AGASA experiment, neither HiRes or Auger have been able so far of detecting anisotropy at any energy or angular scale [?, 81, 111].

At energies around 1 EeV, i.e., the beginning of the ankle where there should still be a sizable Galactic contribution to the flux, Flys Eye has encountered a but statistically significant correlation with the Galactic plane in the energy range between 0.2 and 3.2 EeV [112]. They assessed the proba-

bility of this result being a statistical fluctuation of an isotropic distribution at  $< 0.06\%$ . The most significant enhancement is in the interval 0.4-1.0 EeV. AGASA, on the other hand has postulated a  $> 4\sigma$  excess towards the direction of the Galactic center [113]. The excess was confirmed in two independent data sets with 18274 and 10933 events in the 1-2 EeV region, with chance probabilities of 0.3 and 0.5% respectively. The  $4.5\sigma$  effect observed corresponds to 506 events detected in a region of the sky where only 413.6 were expected. Associated with this enhancement was a probably dipolar signal towards the inner regions of the Galaxy of amplitude 0.04 [114]. An independent confirmation of an anisotropy likely related with this one comes from the SUGAR experiment [115] which, different from AGASA, was able to look directly at the Galactic center. Unfortunately, these findings have not been confirmed so far by either HiRes or Auger [116].

At small scales,  $< 2.5^\circ$ , comparable with the resolution of the experiment, AGASA has postulated the existence of pairs and triplets of events, which have grown in number over the years to a total of 7 pairs and 1 triplet (or 9 pairs if the triplets is counted as 2 pairs) above 40 EeV [?, 121, 122, 123]. Since, following AGASA estimations, a total of 1.7 pairs was expected at this separation, the results has a chance probability of less than 0.1%. This result has not been confirmed by HiRes in the combined AGASA-HiRes data set [124], but still remains a topic of hot debate due to its enormous astrophysical significance. It must also be noted that it is difficult to understand simultaneously the existence of at least the three original pairs when the actual distribution of matter inside the GZK sphere is taken into account [93].

Finally, another very promising anisotropic signal coming from the AGASA experiment is found as an alignment in the relative orientation of pairs of incoming events above 10 EeV in the  $\Delta l-\Delta b$  plane (Galactic coordinates) on scales of  $\lesssim 10^\circ$  [117, 118]. It must be noted that this anisotropy is fundamentally different from a simple clustering of events in a given angular scale, since it is limited to an aligned structure in the two point correlation function. This signal can only be produced as the result of charged CR bending their trajectories in the Galactic magnetic field. The astrophysical implications of this observation have been analyzed in detail in [119]. CR polarization, if confirmed, could turn into a powerful tool for the determination of the number of nearby CR point sources and for imposing constraints on the intensity and topology of the Galactic and extragalactic magnetic fields.

Summing up the results on anisotropy at the highest energies so far, and remembering our discussion about the effects of different spacial structures and intensities of the IGMF (sections 5.1 and 5.2), the high degree of isotropy observed so far by most experiments, seems to favor a laminar IGMF structure. However, it must be remembered that local coherent magnetized structures, as our own Halo could be, may be able to de-focus particles coming from point sources into an apparently isotropic flux [125, 126] further complicating the analysis.

## References

1. Nagano M. and Watson A. A., *Rev. Mod. Phys.* 72 (2000) 689.
2. Nagano M. et al., *J. Phys. G* 10, 1295 (1984).
3. Pravdin M. I. et al., *Proc. 26th Int. Cosmic Ray Conf. (Salt Lake City)* 3 (1999) 292.
4. M.I. Pravdin et al., *Proc. 28th Int. Cosmic Ray Conf.(Tuskuba)* (2003) 389
5. Bird D. J. et al., *Phys. Rev. Lett.* 71 (1993) 3401.
6. Bird D. J. et al., *Astrophys. J.* 441 (1995) 144.
7. Abu-Zayyad T. et al., *Astrophys. J.* 557 (2001) 686.
8. Ave M. et al., *Proc. 27th Int. Cosmic Ray Conf. (Hamburg)* 1 (2001) 381, See also astro-ph/0112253.
9. Takeda M. et al., *Astropart. Phys.* 19 (2003) 447.
10. HiRes Collaboration, *Phys. Rev. Letters* 92, 151101 (2004).
11. Han J. L., (2001) astro-ph/0110319.
12. Watson A. A., *Nuclear Physics B (Proc. Suppl.)* 136 (2004) 290
13. Linsley, J., *Proc 15th Int Cos Ray Conf (Plovdiv)* 12 (1977) 89
14. Zha, M., J Knapp and S Ostapchenko, *Proc 28th Int Cos Ray Conf (Tsukuba)* 2 (2003) 515.
15. Gaisser, T.K., et al., *Phys Rev D* 47 (1993) 1919
16. Archbold, G. et al., *Proc. 28th Int Cos Ray Conf (Tsukuba)* 1 (2003) 405
17. Shinosaki, K., for the AGASA group, *Nuclear Physics B (Proc. Suppl.)* 136 (2004) xxx
18. Hayshida: Akeno/AGASA muons
19. Antoni et al, *Nuclear Instruments and Methods in Physics Research A* 513 (2003) 490-51
20. Badea A. F. et al., *Nuclear Physics B (Proc. Suppl.)* 136 (2004) 384-389
21. Kampert, K.-H., et al. *Nuclear Physics B (Proc. Suppl.)* 136 (2004) 273-281
22. Antoni T. et al, *Nucl. Inst. Meth. A* 513 (2003) 490.
23. Navarra G. et al, *Nucl. Inst. Meth. A* 518 (2004) 207.
24. Linsley, J., *Proc 18th ICRC, Bangalore*, 12 (1983) 144.
25. Song, C., et al., *Astropart Phys* 14 (2000) 7.
26. Ave M., et al., *Astroparticle Physics* 1961 (2003), and astro-ph/0203150
27. Dova M. T. et al., *Astropart. Phys.* 21, 597 (2004).
28. Ave, M., et al., *Proc 28th Int Cos Ray Conf (Tsukuba)* 1 (2003) 349.
29. Tiba A., Medina Tanco G. A., and Sciutto S. J., astro-ph/0502255.
30. Abu-Zayyad T. et al., *ApJ* 557 (2001) 686.
31. Shinozaki K. & Teshima M., *Nuclear Physics B (Proc. Suppl.)* 136 (2004) 18.
32. Shinozaki K. et al., *ApJ Lett.*, 571 (2002) 117.
33. Risse M., *29th ICRC, Pune*, 7 (2005) 143.
34. Pierre Auger Collaboration, *29th ICRC, Pune*, 7 (2005) 147.
35. M. Ave et al., *Phys. Rev. Lett.* 85, 2244 (2000)
36. M. Ave et al., *Phys. Rev. D* 65, 063007 (2002).
37. G. Gelmini, O.E. Kalashev, and D.V. Semikoz, astro-ph/0506128 (2005), and references therein.
38. Ptuskin V.S., Rapporteur Talk, *29th ICRC, Pune*, 10 (2005) 317.
39. Meyer J. P. et al., *ApJ* 487 (1997) 182.
40. Blasi P., Epstein R. I. & Olinto A. V., astro-ph/9912240.
41. Medina Tanco G. A. and Watson A. A., *27th ICRC, Hamburg* (2001) 531.



42. Medina Tanco G. A. et al., ApJ, 492 (1998) 200.
43. Kronberg P. P., Rep. Prog. Phys. 57 (1994) 325.
44. Berezhinsky V. S., Bulanov S., Dogiel V., Ginzburg V., Ptuskin V., "Astrophysics of Cosmic Rays" 1990, North-Holland Publishing Company, Amsterdam (ISBN: 0444886419)
45. Berezhinsky V. S. & Grigoreva S. I., A & A 199 (1988) 1.
46. Greisen, K., Phys. Rev. Lett., 16 (1966) 748
47. Zatsepin, G. T., & Kuzmin, V. A., Pisma Zh. Eksp. Teor. Fiz., 4 (1966) 114
48. Berezhinsky V., Gazizov A. Z., Grigorieva S. I., astro-ph/0502550.
49. Lemoine, M., Phys. Rev. D71 (2005) 083007
50. Stanev T., arXiv:astro-ph/0303123;
51. Stanev T., Seckel D. & Engel R., Phys. Rev. D 68 (2003) 103004
52. Stanev T. et al., Phys. Rev. D 62 (2000) 093005
53. Medina Tanco, G., in Physics and Astrophysics of UHECRs, eds M. Lemoine & G. Sigl, Lect. Notes in Phys., 576 (2001) 155.
54. Medina Tanco G. A., et al, Astroparticle Physics, 6 (1997) 337.
55. Medina Tanco G. A. & Ensslin T. A., Astroparticle Phys. 16(2001)47.
56. Medina Tanco G. A., Ap. J. 549 (2001) 711.
57. Medina Tanco G. A., Ap. J. Letters, 505 (1988) L79.
58. Medina Tanco, G. A., proc. of the 25th ICRC, Durban, South Africa, 4(1997)477.
59. Aloisio R. & Berezhinsky V. S., Astrophys. J., 625 (2005) 249.
60. Berezhinsky, V. S., Grigorieva S. I. and Hnatyk B. I., Astroparticle Phys., 21 (2004) 617.
61. Abbasi R. U. et al., Astroparticle Phys., 23 (2005) 157.
62. De Marco D. et al., Astroparticle Phys. 20 (2003) 53.
63. Auger Collaboration, Nuc. Inst. Methods A, 523 (2004) 50.
64. Auger Collaboration, 29th ICRC Pune, 7 (2005) 387.
65. Bordes J. et al., Astropart. Phys. 8 (1998) 135.
66. Jain P. , McKay D.W., Panda S., Ralston J.P., Phys. Lett. B484 (2000) 267.
67. Chung D. et al., Phys. Rev. D57 (1998) 4606.
68. Sato H., Tati T., Prog. Theor. Phys., 47 (1972) 1788.
69. Kirzhnits D. A., Chechin V. A., Yad. Fiz. 15 (1972) 1051.
70. Coleman S., Glashow S. L., Phys. Rev. D 59 (1999) 116008.
71. Aloisio R. et al., Phys. Rev. D 62 (2000) 053010.
72. Alfaro J., Palma G., Phys. Rev. D, 67 (2003) 083003.
73. Bhattacharjee P., Sigl G., Phys. Rept.327, 109 (2000) [arXiv:astro-ph/9811011].
74. Berezhinsky V. S., Nucl. Phys. (Proc. Suppl) B87, 387 (2000).
75. Kuzmin V.A. and Tkachev I.I., Phys. Rep. 320, 199 (1999).
76. Aloisio R., Berezhinsky V., Kachelriess M., Nucl. Phys. B, 136 (2004) 319.
77. Sarkar S., Toldra R., Nucl. Phys. B 621 (2002) 495.
78. Linsley J., Phys. Rev. Lett. 10 (1963)146.
79. Linsley J., AIP Conf. Proc. 433 (1998) 1.
80. Bird, D., et al., 1995, Astrophys. J. 441, 144.
81. Auger Collaboration, 29th ICRC Pune, 10 (2005) 115.
82. Rubtsov G. I. et al., PRD 73 (2006) 063009.
83. Bertone G., Isola C., Lemoine M., Sigl G., Phys. Rev. D66 (2002) 103003.
84. Allard D. et al., astro-ph/0505566.
85. Yamamoto T. et al. Astropart.Phys. 20 (2004) 405.

86. Arp, H., Phys. Lett. A 129 (1988) 135
87. Auger Design Report, 1996
88. Berezhinsky V. S. and Grigoreva, S. I., A & A, 199 (1988) 1.
89. Blanton, M., P., B., and V., O. A., 2000, astro-ph/0009466
90. Kim, K.-T., Kronberg, P. P., G., G., and T., V., 1989, Nature 341, 720
91. Medina Tanco, G. A., 1997b, in 25th ICRC, Vol. 4, p. 481
92. Medina Tanco, G. A., 1997c, in 25th ICRC, Vol. 4, p. 477
93. Medina Tanco, G. A., 1998a, Astrophys. J. Lett. 495, L71
94. Medina Tanco, G. A., 1998b, Astrophys. J. Lett. 505, L79
95. Medina Tanco, G. A., 1999, in Proc. 16th ECRC, Alcalá de Henares, Espanha (J. Medina ed. ), pp 295–298
96. Medina-Tanco, G. A., 1999, Astrophys. J. Lett. 510, L91
97. Medina Tanco, G. A., 2000b, astro-ph/9809219, in Topics in Cosmic Ray Astrophysics, M. Duvernois (ed.), Nova Science Pub. Inc., New York. p. 299
98. Medina Tanco G. A., 2001, ApJ 549 (2001) 711, astro-ph/0011454.
99. Medina Tanco, G. A. and Enßlin, T. A., 2001, Astroparticle Physics (in Press), astro-ph/0011454
100. Ryu, D., Kang, H., and Biermann, P. L., 1998, Astronomy and Astrophys. 335, 19
101. Vallee, J. P., 1997, Fundamentals of Cosmic Physics 19, 1
102. Yoshida, S. and Teshima, M., Prog. Theor. Phys. 89 (1993) 833.
103. Stecker, F. W. and H., S. M., 1999, ApJ 512 (1999) 521.
104. Sigl G., Lemoine M., Biermann P. L., Astropart. Phys. 10 (1999) 141.
105. Lemoine M., Sigl G., Biermann P. L., astro-ph/9903124.
106. Watson A. A., Adv. Sp. Res. 4 (1984) 35.
107. Watson A. A., Nucl. Phys. B Suppl, 22B (1991) 116.
108. Takeda M. et al., ApJ 522 (1999) 225.
109. Shinozaki K., Teshima M., Nuclear Physics B (Proc. Suppl.), 136 (2004) 18.
110. HiRes Collaboration, Nuclear Physics B (Proc. Suppl.) 138 (2005) 307.
111. Auger Collaboration, 29th ICRC Pune, 7 (2005) 75.
112. Bird D. J. et al., ApJ, 511 (1999) 739.
113. AGASA coll. (1998), Astropart.Phys. 10 (1999) 303-311, astro-ph/9807045.
114. Teshima M. et al., 27th ICRC Hamburg (2001).
115. Bellido, J. A. et al., Astropart. Phys., 15 (2001) 167
116. Auger Collaboration, 29th ICRC Pune, 7 (2005) 67.
117. Takeda, M. et al., 27th ICRC. Hamburg, 1 (2001) 345.
118. Teshima M. et al., 28th ICRC. Tsukuba, 1 (2003) 401.
119. Medina Tanco G. A., Teshima M. Takeda M., 28th ICRC Tsukuba (2003)
120. Takeda, M. et al., Phys. Rev. Lett. 81 (1998) 1183.
121. Takeda, M. et al., Astrophys. J. 522 (1999) 225.
122. Takeda, M. et al., Proc. 27th ICRC Hamburg 1 (2001) 345.
123. Teshima M. et al., Proc. 28th ICRC Tsukuba, 1 (2003) 401.
124. Abbasi R. U., ApJ 623 (2005) 164.
125. Ahn E. J., Medina-Tanco G., Biermann P. L., Stanev T., astro-ph/9911123.
126. Biermann P. L., Ahn E. J., Medina Tanco G., Stanev T., Nucl. Phys. Proc. Suppl. 87 (2000) 417 astro-ph/0008063].